

Quantifying Shear-Induced Deformation and Detachment of Individual Adherent Sickle Red Blood Cells

Yixiang Deng,^{1,2} Dimitrios P. Papageorgiou,³ Hung-Yu Chang,¹ Sabia Z. Abidi,^{3,4} Xuejin Li,^{1,5,*} Ming Dao,³ and George Em Karniadakis^{1,*}

¹Division of Applied Mathematics and ²School of Engineering, Brown University, Providence, Rhode Island; ³Department of Materials Science and Engineering, Massachusetts Institute of Technology, Cambridge, Massachusetts; ⁴Department of Bioengineering, Rice University, Houston, Texas; and ⁵Department of Engineering Mechanics, Key Laboratory of Soft Machines and Smart Devices of Zhejiang Province, Zhejiang University, Hangzhou, People's Republic of China

ABSTRACT Vaso-occlusive crisis, a common painful complication of sickle cell disease, is a complex process triggered by intercellular adhesive interactions among blood cells and the endothelium in all human organs (e.g., the oxygen-rich lung as well as hypoxic systems such as liver and kidneys). We present a combined experimental-computational study to quantify the adhesive characteristics of sickle mature erythrocytes (SMEs) and irreversibly sickled cells (ISCs) under flow conditions mimicking those in postcapillary venules. We employed an in vitro microfluidic cell adherence assay, which is coated uniformly with fibronectin. We investigated the adhesion dynamics of SMEs and ISCs in pulsatile flow under well-controlled hypoxic conditions, inferring the cell adhesion strength by increasing the flow rate (or wall shear stress (WSS)) until the onset of cell detachment. In parallel, we performed simulations of individual SMEs and ISCs under shear. We introduced two metrics to quantify the adhesion process, the cell aspect ratio (AR) as a function of WSS and its rate of change (the dynamic deformability index). We found that the AR of SMEs decreases significantly with the increase of WSS, consistent between the experiments and simulations. In contrast, the AR of ISCs remains constant in time and independent of the flow rate. The critical WSS value for detaching a single SME in oxygenated state is in the range of 3.9–5.5 Pa depending on the number of adhesion sites; the critical WSS value for ISCs is lower than that of SMEs. Our simulations show that the critical WSS value for SMEs in deoxygenated state is above 6.2 Pa (multiple adhesion sites), which is greater than their oxygenated counterparts. We investigated the effect of cell shear modulus on the detachment process; we found that for the same cell adhesion spring constant, the higher shear modulus leads to an earlier cell detachment from the functionalized surface. These findings may aid in the understanding of individual roles of sickle cell types in sickle cell disease vaso-occlusion.

INTRODUCTION

Sickle cell disease (SCD), one of the most common inherited blood disorders, is characterized by hemolytic anemia, vaso-occlusion, and organ damage (1,2). SCD results from a point mutation of the β -globin gene that leads to the mutated sickle hemoglobin (HbS), which polymerizes upon deoxygenation (3,4). Intracellular polymerization of HbS leads to decreased deformability of red blood cells (RBCs) as well as cell membrane damage resulting in het-

erogeneous RBC shapes, including elongated, granular, oval, holly-leaf, and crescent (classic sickle) shapes (5–9). The sickled RBCs become dehydrated, inflexible, and abnormally adhesive (10,11). These characteristics promote vaso-occlusion because of intercellular adhesive interactions among RBCs, white blood cells (WBCs), platelets, and endothelium (12–15). Recent in vivo and in vitro studies have also indicated mechanistic differences between SCD vaso-occlusions in oxygen-rich organs (such as lung) and hypoxic (systemic) organs (such as kidney and liver) in which the hypoxia conditions are very different with respect to blood flow and local vascular geometries (15–17).

It has been demonstrated that both the mechanical properties and shape heterogeneity of sickle RBCs play a role in cell adhesion (18,19). In earlier studies, considerable uncertainty existed with respect to the dependence of adhesive

Submitted August 15, 2018, and accepted for publication December 10, 2018.

*Correspondence: xuejin_li@zju.edu.cn or george_karniadakis@brown.edu

Yixiang Deng and Dimitrios P. Papageorgiou contributed equally to this work.

Editor: Mark Alber.

<https://doi.org/10.1016/j.bpj.2018.12.008>

© 2018 Biophysical Society.

strength of sickle RBCs on these two factors: in a static system, the high-density rigid sickle RBCs were found to be the most adherent (20); by contrast, in a shear flow system, these high-density rigid RBCs show less adhesion to endothelial cells than the low-density deformable sickle RBCs (21), resulting from the irregular geometry and decreased deformability that prevents the cell membrane receptors from interacting with the ligands. However, after an incubation period to allow more time for sickle RBCs to form attachments to the endothelial cells, the high-density rigid sickle RBCs could become more adherent as they exhibit a greater number of adhesion sites compared to those of low-density deformable ones (22).

Computational modeling and simulations of all blood cell adhesion dynamics have improved considerably in recent years (23–27), helping to enhance our understanding of the underlying cytoadherence mechanisms at the molecular and cellular levels. Here, we briefly describe a few of the major achievements. The precursory work was presented by Bell (28) and Dembo (29), who developed kinetic cell adhesion models to investigate the kinetics of receptor-ligand interactions under external forces. These kinetic models and their extensions have been commonly applied to examine the dynamics of cell adhesion (30–35). In SCD, a combination of different RBC models (36–39) with HbS fiber growth models (40–42) allows simulations of shape change and adhesive properties of hypoxia-affected sickled RBCs under static conditions; however, it becomes computationally prohibitive when modeling cell adhesion under flow conditions. In our previous simulations, we have successfully applied a multiscale RBC (MS-RBC) model (43,44) to examine the adhesion dynamics of sickle RBCs (45) and probe the vaso-occlusion phenomena in SCD (46). We concluded that 1) given the same adhesion potential for low-density deformable sickle RBCs and high-density rigid sickle RBCs, the adhesive force magnitude exhibits an inverse relationship with cell rigidity (45); and 2) the vaso-occlusion mechanisms are multifaceted and multistage in nature. The intercellular RBCs/WBCs and WBCs/endothelium adhesion as well as HbS polymerization induced RBC shape, and deformability changes play critical roles in determining the magnitude of SCD vaso-occlusion (46).

Advances in experimental techniques, including single-molecule atomic force microscopy experiments (47,48) and microfluidics (49), have allowed accurate measurements of sickle RBC adhesion. These experimental measurements reveal that sickle RBCs exhibit enhanced adhesion in hypoxia (22,50,51), and therapy with hydroxyurea (HU) reduces the adhesion of sickle RBCs to endothelial cells (47,48). Despite these previous studies, the complex nature of the adhesion mechanisms leading to vaso-occlusion, have not been fully elucidated. Hence, further quantification of the adhesion characteristics of sickle RBCs can improve our understanding of the SCD pathophysiology. This consideration

leads to the following questions: how do low-density deformable adherent sickle RBCs and high-density rigid ones behave differently when subjected to pulsatile flow with variable shear stress, especially in hypoxic conditions? What is the magnitude of the corresponding adhesion force? Recently, we have developed an in vitro microfluidic RBC adherence assay (52). This platform provided measurements of cell adhesion dynamics under flow conditions mimicking those in postcapillary venules. This device also enables a controllable way of inferring RBC adhesion strength by gradually increasing shear flow stress until the onset of cell detachment (53). In this study, we perform microfluidic experiments and companion computations to investigate sickle RBC detachment dynamics under physiologically relevant flow and hypoxic conditions.

MATERIALS AND METHODS

Experiments

Deidentified blood samples from six homozygous for HbS SCD patients at the University of Pittsburgh Medical Center were selected for this study after institutional review board approvals from the University of Pittsburgh (institutional review board protocol PRO08110422). The six samples comprised four samples with HU treatment and two samples without HU treatment. All samples were collected into 4 mL potassium-ethylenediaminetetraacetic acid (K2-EDTA) spray-coated anticoagulant vacutainers (7.2 mg), shipped to Massachusetts Institute of Technology on melting ice by overnight delivery and stored at 4°C. After removal of the buffy coat and blood plasma, the packed RBCs were washed twice with Dulbecco's phosphate buffer saline (Thermo Scientific, Waltham, MA) for 5 min and were resuspended in Dulbecco's phosphate buffer saline medium with 1% (w/v) bovine serum albumin (EMD Millipore, Danvers, MA) at a concentration of 2–3 μL packed RBCs per 200 μL medium solution. Thus, the estimated hematocrit of the RBC suspensions used within the microfluidic channels is ~ 1.0 – 1.5% .

To study the adhesion dynamics of sickle RBCs under shear flow and hypoxia, we conducted experiments of RBC suspensions in a specially developed hypoxic microfluidic device (7,52), which is comprised of a free-standing gas-permeable polydimethylsiloxane membrane ($H_{\text{PDMS}} = 150 \mu\text{m}$) within a dual-layer microchannel construction. The dual-layer device consists of a "flow microchannel" ($D_{\text{flow}} = 15 \mu\text{m}$) in which there was flow of an RBC suspension and a "gas microchannel" ($D_{\text{gas}} = 100 \mu\text{m}$) in which the desired gas mixture of carbon dioxide (CO_2), oxygen (O_2) and nitrogen (N_2) was delivered. The flow channel's walls were functionalized with fibronectin (FN), and the rectangular cross section at the region of interest (ROI) had an equivalent hydraulic diameter of $D_h \approx 30 \mu\text{m}$. In addition, both flow and gas microchannels were $L = 3 \text{ mm}$ in length and $W = 1.326 \text{ mm}$ in width and connected with in-line pressure and flow sensors, which allows us to precisely control the oxygen level of the RBC's microenvironment as well as the flow rate (Q) within the devices' ROI. Based on the wall shear stress (WSS) calculations in (54,55), we obtain the WSS $\tau_w = 3\eta \times Q/W \times D_{\text{flow}}^2$, where $\eta = 7.0 \text{ Pa}\cdot\text{s} \times 10^{-4}$ is the fluid viscosity. In our study, the flow rate Q takes values between 0 and 67.5 $\mu\text{L}/\text{min}$, and hence, τ_w ranges from 0 to 7.91 Pa.

The microfluidic device imaging was performed using Zeiss Axiovert 200 (Zeiss, Oberkochen, Germany) and Olympus IX71 inverted microscopes (Olympus, Tokyo, Japan). Hitachi KP-D20A charge-coupled device (752p \times 582 p; Hitachi, Tokyo, Japan) and Olympus DP72 cameras were used for image acquisition. All testing was performed at 37°C using a heating incubator (ibidi heating system; ibidi USA, Fitchburg, WI). Furthermore, to enhance the imaging contrast of RBCs, (i.e., to isolate

the information carried by the hemoglobin at 410 and 430 nm), a 414/46-nm single-band bandpass filter was used (Semrock, Rochester, NY). Here, we consider two types of sickle RBCs (i.e., sickle mature erythrocytes (SMEs) and irreversibly sickle cells (ISCs)). Specifically, we consider two different types of SMEs, namely SME1 and SME2, as explained in detail in (52). In brief, SME1s are cells that exhibit significant shape change under hypoxia, whereas SME2s largely maintain their normoxia shape even under hypoxia (52). After a period of static incubation to allow the sickle RBCs to settle and adhere to the FN-coated wall, we started adjusting the flow rate (or shear stress) within the ROI via flow pulses. Increasing flow rate pulses impose corresponding increasing shear stress on the adherent RBCs. In this study, a typical pulse period for an adhered cell exposed to a particular shear stress is $\sim 2\text{--}4$ s. For each respective flow rate value, the cell aspect ratio (AR) and dynamic deformability index (DDI) were measured. After that, the critical WSS (τ_w^c) for detaching a sickle RBC from the substrate was recorded, which was then used to evaluate and quantify the strength of cell adhesion to substrates. In experiments, it remains a challenge to measure the hydrodynamic drag force on adhered cells directly. For simplicity, the drag force is referred to as the equivalent shear force (F_{cs}) that drives the cell away from the adherent substrate. In the current study, F_{cs} is approximated by $A_{cs}\tau_w$, where A_{cs} is the cell-substrate contact area. We examined the cell dynamics in response to WSS by real-time monitoring of in vitro behavior of individual sickle RBCs under pulsatile flow by tuning the fluid flow rate. For further details on the microfluidic device fabrication, protein functionalization and experimental setup, see (7.52).

Simulation model and method

MS-RBC model

Following our previous computational studies (45,46), we employ the MS-RBC model to simulate the adhesion dynamics of sickle RBCs under pulsatile flow conditions. In the MS-RBC model, the RBC membrane is modeled by a two-dimensional triangulated network with N_v vertices connected by N_s edges and N_t triangles. In this study, the elastic energy of the spring bonds is represented by the following:

$$V_s = \sum_{j \in 1 \dots N_s} \left[\frac{k_B T l_m (3x_j^2 - 2x_j^3)}{4p(1-x_j)} + \frac{k_p}{(n-1)l_j^{n-1}} \right], \quad (1)$$

where p is the persistence length, l_i is the length of spring i , l_0 , and l_m are the equilibrium spring length and maximal spring extension, and $k_B T$ is the energy unit. The bending resistance of the RBC membrane is modeled by the following:

$$V_b = \sum_{\alpha, \beta \text{ pair}} k_b [1 - \cos(\theta_{\alpha\beta} - \theta_0)], \quad (2)$$

where k_b is the bending modulus constant, $\theta_{\alpha\beta}$ is the instantaneous angle between two adjacent triangles having common edge, and θ_0 is the spontaneous angle.

In addition, the RBC model includes the area and volume conservation constraints, which mimic the area incompressibility of the lipid bilayer and the incompressibility of the interior fluid, respectively. The corresponding energy terms are given by the following:

$$V_{a+v} = \sum_{j \in 1 \dots N_t} \frac{k_a (A_j - A_0)^2}{2A_0} + \frac{k_a (A - A_0^{\text{tot}})^2}{2A_0^{\text{tot}}} + \frac{k_v (V - V_0^{\text{tot}})^2}{2V_0^{\text{tot}}}, \quad (3)$$

where k_a and k_v are the area and volume constraint coefficients, A_0 is the triangle area, and A_0^{tot} and V_0^{tot} are the total area and volume of a RBC, respectively.

Using the MS-RBC model, we have developed a unified modeling framework for blood flow simulations, which has been validated in a number of computational simulations of blood flow in normal and pathological conditions (56,57), including malaria (58), sickle cell anemia (46,59), hereditary spherocytosis (60), and diabetes mellitus (61,62).

Cell adhesion model

We employ a particle-based stochastic bond formation/dissociation model (30,33) to capture the effective adhesive interactions between RBCs and FN-coated substrates. At each time step Δt , transient adhesive bonds can be formed between RBCs and substrates with probability $P_{on} = 1 - e^{-k_{on}\Delta t}$ within a characteristic length d_{on} , whereas the existing adhesive bonds can be ruptured with probability $P_{off} = 1 - e^{-k_{off}\Delta t}$ within a critical length d_{off} , where k_{on} and k_{off} are bond formation and dissociation rates defined by the following:

$$k_{on} = k_{on}^0 \exp\left(-\frac{\sigma_{on}(l-l_0)^2}{2k_B T}\right) \text{ and} \quad (4)$$

$$k_{off} = k_{off}^0 \exp\left(-\frac{\sigma_{off}(l-l_0)^2}{2k_B T}\right),$$

where k_{on}^0 and k_{off}^0 are the unloaded bond formation and dissociation rates, and σ_{on} and σ_{off} are the effective formation and rupture strengths, respectively. For existing adhesive bonds, the adhesive force between RBC and substrates is given by $F(l) = 2k_s(l-l_0)$, where k_s is the adhesion spring constant and l_0 the equilibrium length. The stochastic adhesion dynamics model has been validated in a number of computational studies, including the investigation of adhesive dynamics of RBCs in malaria (33,58) and SCD (45,46). In this study, parameters related to the adhesive parameters between sickle RBCs and substrates are summarized in Table 1.

Pulsatile flow

Such flow is generated by imposing a pressure gradient (with a sudden rise followed by a sudden fall) on the fluid flow inside a 40- μm -long, 20- μm -wide, and 24- μm -high microchannel between two parallel solid walls, which are modeled by freezing layers of particles with bounce-back reflection to satisfy the no-slip boundary condition (63). To model the adhesive ligands, we coated the solid walls with static particles (Fig. 1 a, green dots), which can potentially interact with the receptors on RBC membrane to form adhesive bonds. In this study, the applied pressure gradient $ac(dp/dx)$ is driving flow in the positive x -direction, as illustrated in Fig. 1 a, and the corresponding velocity component is given by the following:

$$v_x = \frac{1}{2\eta} \frac{dP}{dx} (hy - y^2), \quad (5)$$

where η is the fluid viscosity and h the distance between the two parallel solid walls. For the cell detachment test, the applied pressure gradient, dP/dx , is raised in each pulse duration by 25–100% to generate a shear flow with τ_w over one order of magnitude (Fig. 1 b). To determine the pressure gradient range applied in the computational simulations, we require that the obtained τ_w values fall within the experimental measured data ranged from 0 to 7.9 Pa. Some dP/dx values in the range of 0–27.6 Pa/m were found to satisfy this requirement (Fig. 1 b). In this way, the adhesion strength of adherent cells can be determined by direct and real-time monitoring of their shape change and dynamic behavior during cell detachment process, and it can be plotted against the critical value of τ_w^c for cell detachment.

TABLE 1 Simulation Parameters for Adhesion Dynamics of Sickle RBCs

Parameters	Simulation	Physical	Reported Range
k_s	100.0–8000.0	(4.8–392.0) $\mu\text{N/m}$	(10^{-5} – 10^{-2}) N/m (30)
l_0	0.0	0.0 μm	(0.0–0.04) μm (46,58,71)
d_{on}	0.15	0.14 μm	(0.1–0.15) μm (46,58)
d_{off}	0.75	0.72 μm	(0.0–0.15) μm (46,72)
σ_{on}	10.58	0.51 $\mu\text{N/m}$	0.5 $\mu\text{N/m}$ (58)
σ_{off}	3.49	0.18 $\mu\text{N/m}$	0.05 $\mu\text{N/m}$ (58)
k_{on}^0	100.0	$1.35 \times 10^4 \text{ s}^{-1}$	(0.1–1.0) $\times 10^4 \text{ s}^{-1}$ (73)
k_{off}^0	~ 0.001 –0.1	(~ 1.35 – 135.0) s^{-1}	(0.5–300) s^{-1} (74)

We note that the adhesion parameters (k_{on}^0 , d_{on} , and $\sigma_{on}/k_B T$) are only applied for the formation of adhesive bonds between RBC and substrates. After that, they are not directly involved in the detachment process and turned off for the modeling of RBC detachment dynamics.

Model setup and parameter estimation

As mentioned previously, sickle RBCs exhibit heterogeneity in adhesion dynamics, which is primarily a consequence of cell density, cell maturity, and deoxygenation (5,6). Specifically, under the deoxygenated conditions, the instantaneous contact area between cells and substrates varies significantly among cells that feature different polymerization kinetics, which directly affects the adhesion strength and adhesion sites (52). Taking these facts into consideration, we examine the detachment dynamics of sickle RBCs with variable cell membrane shear modulus (μ), adhesion spring constant (k_s), and number of adhesion sites.

In this study, we use the MS-RBC model to simulate a sickle RBC in shear flow with the following features: $N_v = 2000$, RBC diameter $D_0 = 7.86 \mu\text{m}$, membrane surface area $A_0^{\text{tot}} = 135.2 \mu\text{m}^2$, and cell volume $V_0^{\text{tot}} = 92.4 \mu\text{m}^3$. Following the experimental study, we consider three types of sickle RBCs (i.e., SME1, SME2, and ISC) under shear flow. Following our previous studies (8,46,52), we set the equivalent shear modulus for SME1s, SME2s, and ISC under the oxygenated and deoxygenated states (see Table 2). We determine the value of k_s parameter by fitting the experimental τ_w values required for cell detachment. We note that the sickle RBCs may detach from the surface under WSS from low (~ 0.2 Pa) to high (~ 7.9 Pa). Here, we choose to present the findings from several representative experiments (the critical values of $\tau_w^{\text{c,EXP}}$ from these selected ones (except for ISCs because they always detach from the wall at low shear) are in the middle of all the experimental values obtained) to guide our cell adhesion models, targeting specifically the hypoxia-induced changes in sickle RBC adhesion. For example, from an individual case selected for ISC under the oxygenated state (Video S1), we found that the estimated value of τ_w required for cell detachment at $k_s = 72.0 \mu\text{N/m}$ is close to the selected experimental data (Shear-Induced Detachment of Sickle RBCs; also see corresponding Video S2). Therefore, we have chosen

$k_s = 72.0 \mu\text{N/m}$ for ISC under the oxygenated state. Similarly, we choose k_s values for ISCs under the deoxygenated state and SME2s under both the oxygenated and deoxygenated states, which are listed in Table 2. It is worth noting that the detachment process is stochastic; hence, it is possible that cells detach at a shear rate lower than τ_w^{c} in longer flow pulses. In fact, in our simulation, we did observe some rare cases that the adhered cells detached before τ_w reaches its critical value. However, given the limitation of computation resources and based on a physiological fact that each cardiac cycle takes around 0.8 s to occur (less than the pulse period used in our study), we did not consider them in our discussion. Here, we pay our attention to the influence of cell shape and deformability characteristics on the detachment process of sickle RBCs.

Regarding the adhesion strength of SME1s corresponding to multiple adhesion sites, we model the RBC membrane with a line attachment between the cell and substrate instead of the single-site attachment, similar to our previous simulations on bilayer-cytoskeletal detachment in channel flow (56). In a previous experimental study by Kasschau et al. (64), they observed that the sickle cells may have two-point attachment to the substrate at low shear stress, whereas they exhibit one-point attachment under high shear stress conditions (before detachment). For simplicity, we chose two (or multiple) anchor sites located on the cell membrane as adhesion sites and adopt a weak-strong dual-binding strategy with weak-binding constant (k_s^{wk}) and strong-binding constant (k_s^{st}) to model cell-substrate adhesion. We consider k_s^{st} to be the main dominant factor in determining the adhesion strength of SME1s. Similar to SME2s and ISCs, we choose $k_s^{\text{st}} = 240.0$ and $328 \mu\text{N/m}$ for SME1s under the oxygenated and deoxygenated states, respectively. For comparison, we set k_s^{wk} values to be roughly one-fourth to one-half of the k_s^{st} values so they can be easily ruptured at low or moderate τ_w . In our study, we choose $k_s^{\text{wk}} = (60$ – $120.0) \mu\text{N/m}$ (oxygenation) and $(80$ – $160.0) \mu\text{N/m}$ (deoxygenation) for SME1s.

All simulations were performed using our modified version of the atomistic code named LAMMPS. It takes 6.5×10^6 time steps for a typical simulation performed in the current study. In terms of computing time, on average, it takes ~ 864 CPU core hours for a typical simulation using the computational resources (Intel Xeon E5-2670 2.6 GHz 64-core processors) at the Center for Computation and Visualization at Brown University.

RESULTS AND DISCUSSION

In this section, we employ the MS-RBC model in conjunction with the stochastic adhesion dynamics model to investigate the detachment dynamics of adherent sickle RBCs. First, we validated the computational hydrodynamic flow against the experimental data obtained from a specific microfluidic device (i.e., the device used for the sickle RBC adhesion dynamics) comprising only a single microbead suspended in fluid flow (see Supporting Materials and

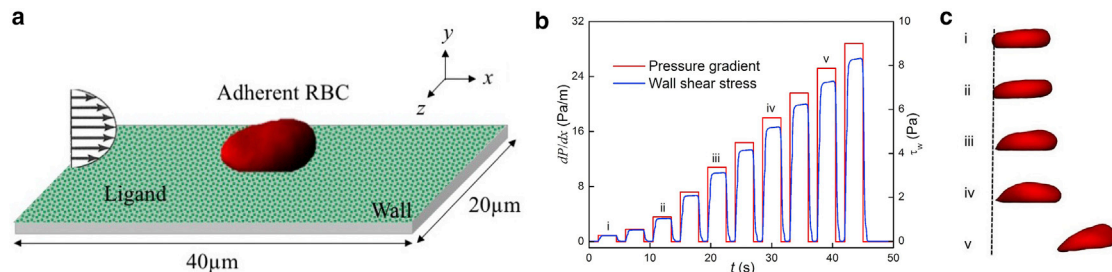


FIGURE 1 Simulation setup for modeling RBC detachment dynamics under pulsatile flow. (a) A schematic representation of an adherent RBC under shear flow. The green surface represents the ligands coated on the vessel wall. (b) Time-dependent pressure gradient (dP/dx) and wall shear stress (WSS) (τ_w) profiles for probing RBC adhesion strength. (c) Shape deformation of an adherent RBC in response to τ_w change (from (i)–(v)). The onset of RBC detachment is shown in (iv). To see this figure in color, go online.

TABLE 2 Overview of Representative Types of Adherent Sickle RBCs in Computational Simulations

Condition	Type	Shear Modulus	Adhesion Sites	Adhesion Spring Constant	Shear Stress Threshold	
		(μ_0)	–	(k_s , $\mu\text{N/m}$)	($\tau_w^{c,\text{EXP}}$, Pa)	($\tau_w^{c,\text{SIM}}$)
Oxy	ISC	100.0	Single	72.0	1.3	1.3
	SME2	1.0	Single	184.0	3.9	4.1
	SME1	1.0	Multiple	$k_s^{wk} = 120.0$	4.9	2.6
	–	–	–	$k_s^{st} = 240.0$	5.5	5.3
DeOxy	ISC	1000.0	Single	72.0	1.2	1.3
	SME2	50.0	Single	42.0	0.9	1.0
	SME1	50.0	Multiple	$k_s^{wk} = 160.0$	(>6.2)	3.5
	–	–	–	$k_s^{st} = 328.0$	(>ac 6.2)	6.7

The symbols Oxy and DeOxy represent the blood samples from SCD patients under the oxygenated (Oxy) and deoxygenated (DeOxy) states. $\mu_0 = 4.73$ pN μm^{-1} is the shear modulus of a healthy RBC. We note that the critical τ_w values are selected from individual sickle cells in several representative experiments, which may be different for a dense suspension of sickle cells. Also, we only train the strong-binding constant k_s^{st} for the SME1s, whereas we set the weak-binding constant k_s^{wk} to be roughly one-fourth to one-half of the k_s^{st} values. The SME1 from SCD blood sample (DeOxy) did not detach by τ_w up to 6.2 Pa, then it recovered its presickle shape after reoxygenation and detached from the surface under the Oxy state.

Methods). Additionally, we performed cross-validation of the numerical results obtained from the force coupling method (65) for the simulation of oscillating flow. After model validation, we simulated the adhesion dynamics of sickle RBCs under shear flow (see Fig. S2), which is analogous to our previous computational studies (33,66). Next, we investigated the detachment dynamics of individual adherent sickle RBCs and performed quantitative analysis of the shape and mechanical factors affecting the cell detachment dynamics. In addition, we also extend our simulations to a complex system containing multiple adherent RBCs with different k_s under shear flow.

Shear-induced detachment of sickle RBCs

In this section, we investigate the shear-induced detachment processes of individual sickle RBCs adhered to fibronectin-coated substrates, under steady normoxia state (oxygenation, 20 vol% O₂) or steady hypoxia state (deoxygenation, 2 vol% O₂) in a fixed field of view within the microfluidic device. We examine the influence of the number of adhesion binding sites (single-site adhesion versus multiple-site adhesion) on the cell detachment dynamics by performing detailed computational simulations and compared with experimentally obtained data.

Under the oxygenated state

The experimental and computational results show an obvious difference in the transient dynamic behavior between the SMEs and ISCs: SMEs (including SME1 and SME2) were observed to deform before detachment from FN-coated substrates under pulsatile flow, whereas ISCs only show little dynamic deformation. These observations suggest that the cell membrane rigidity plays an important role in determining cell adhesion strength, as discussed below.

Single-site adhesion of ISCs and SME2s. Fig. 2, a and b show snapshots of the single-site detachment dynamics of

the ISC versus SME2 in pulsatile flow with increasing shear stress amplitude under the oxygenated state. Before the onset of cell detachment, the key difference in the dynamic behavior of the ISC compared to the SME2 is the elongation profile: the ISC is subject to a very small distortion even under comparably higher shear stress (Fig. 2 a); however, the SME2 experiences a continuing distortion before detachment (Fig. 2 b). When the applied WSS is sufficiently high to overcome the cell adhesion strength, both the ISC and SME2 detach from the substrate.

Multiple-site adhesion of SME1s. Fig. 2 c shows snapshots of the shear-induced deformation of sickle RBCs with multiple-site adhesion and subsequent detachment under the oxygenated state (also see corresponding Videos S3 (experiment, EXP) and S4 (simulation, SIM)). From these experiments and simulations, the following observations are made: the adherent SME1 is deformed when subjected to a pulsatile flow with increasing amplitude of τ_w . We observed that at a sharp increase of fluid flow (or τ_w), the SME1 deforms in a folded shape and the underlying adhesion sites are revealed (Fig. 2 c, white and yellow dotted circles). After that, at the value of $\tau_w \approx 4.9$ Pa (EXP) and 2.6 Pa (SIM) the weaker adhesion site (yellow dotted circle) is ruptured and the cell holds on to the stronger adhesion site (Fig. 2 c, white dotted circle; see also Videos S3 (EXP) and S4 (SIM)). Subsequently, under shear, the RBC attains an elongated shape that is like a teardrop with single-site adhesion. Finally, the cell detaches from the substrate when the applied shear stress is above the threshold ($\tau_w^c \approx 5.5$ Pa (EXP) and 5.3 Pa (SIM)). The transition from two-site (or multiple-site) attachment to single-site attachment during the cell detachment process is in accordance with previous experiment using detachment assays (64).

Quantification. To quantify the effect of the shear stress amplitude on cell deformation, we examine the elastic deformation of sickle RBCs under shear. In this study, the shear-induced elastic deformation of individual sickle RBCs is expressed as an AR defined by $\text{AR} = D_T/D_A$, where

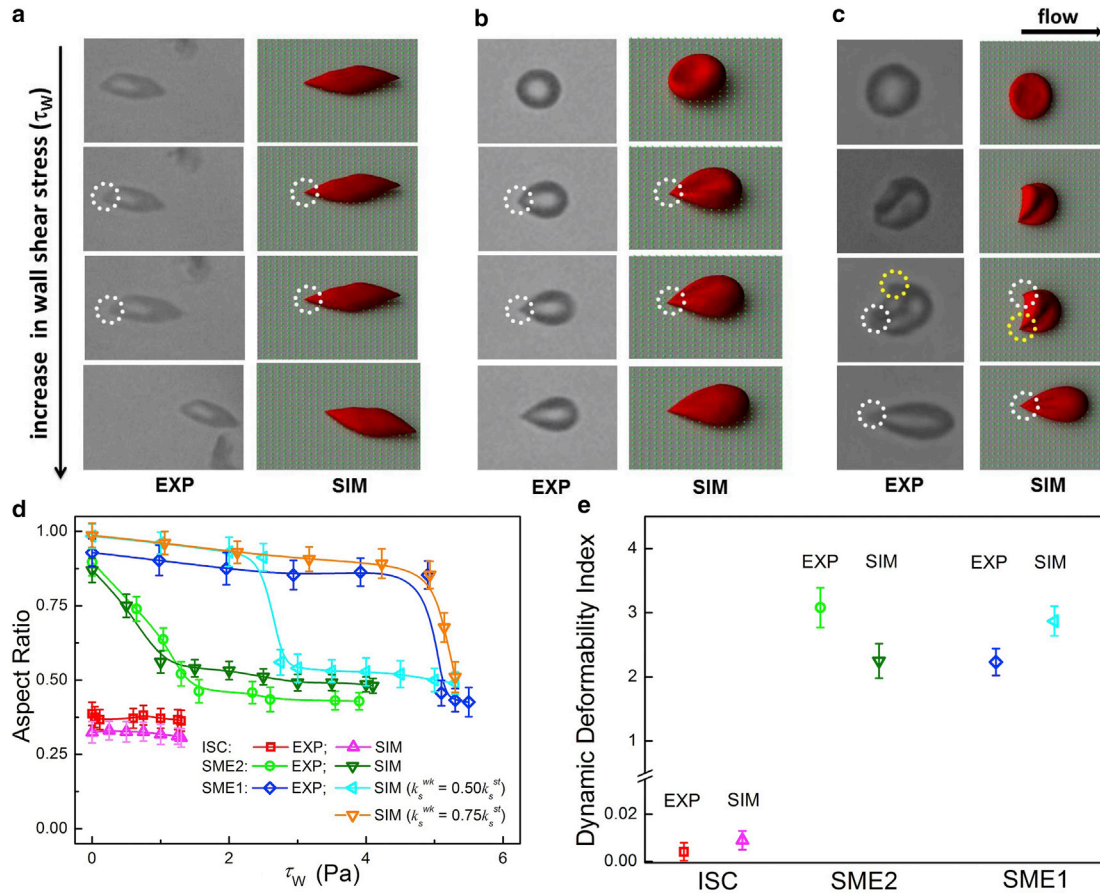


FIGURE 2 Detachment dynamics of sickle RBCs under the oxygenated states. (a–c) Time sequence of adherent ISC ((a) single-site attachment), SME2 ((b) single-site attachment) and SME1 ((c) multiple-site attachment) in response to applied shear stress obtained from experiments (left) and simulations (right). White and yellow dotted circles show the location of adhesion sites. (d) Functional dependence of the aspect ratio (AR) of sickle RBCs on the wall shear stress (WSS) τ_w . (e) Dynamic deformability index of sickle RBCs. The error bars in the figure show the statistical error of a set of measured AR and DDI values of RBCs at different pulse period. To see this figure in color, go online.

D_A and D_T represent the major and minor axes of the deformed RBC. Fig. 2 d shows a plot of the experimental AR change and companion simulation results for the adherent SMEs versus ISCs. With the increase of flow rate (or τ_w), the AR value of SME2s drops rapidly with time, which is indicative of a drastic RBC deformation. Afterward, the AR value becomes fairly constant with τ_w (before the flow becomes fully developed) (Fig. 2 d, green circles and olive down-pointing triangles). The cell detachment occurs when the value of WSS is above the following threshold: $\tau_w^c \approx 3.9$ Pa (EXP) and 4.1 Pa (SIM). For SME1, the AR values decrease slightly with applied WSS at low τ_w ; however, there is a sharp, sudden decrease in AR values immediately after the rupture of the weaker adhesion sites. After that, the AR values smoothly approach saturation at high τ_w (Fig. 2 d, blue diamonds and cyan left-pointing triangles). We find the simulations capture the essential behavior of the multi-adhesion site cases, whereas the difference is due to the relatively low k_s^{wk} chosen (in the range from $1/4(k_s^{st})$ to $1/2(k_s^{st})$) for SME1. If higher k_s^{wk} (e.g., $k_s^{wk} = 3/4(k_s^{st})$) is chosen in this case as observed

experimentally (in Table 2), the simulation curve would be close to the experimental curve (Fig. 2 d, orange right-pointing triangles; see also Video S5). By contrast, the AR value of ISC remains moderately unaltered up to the point of cell detachment (Fig. 2 d, red squares and magenta up-pointing triangles). We verified that the ISCs are less adherent to FN-coated substrates as compared to the SME2s (i.e., in experiments we measured $\tau_w^c \approx 1.3$ Pa, and in simulations, we computed roughly the same value.

In addition, we characterized the adherent cell deformation by the DDI, which is defined as the rate of AR change in response to the increase of τ_w (50). Fig. 2 e shows that the DDI values of ISCs are significantly lower compared to those of SME1s and SME2s.

Under the deoxygenated state

The detachment dynamics of ISCs under the deoxygenated state is quite similar to that of ISCs under the oxygenated state, so we shall not discuss here. Next, we focus our attention on the shape deformation and detachment dynamics of

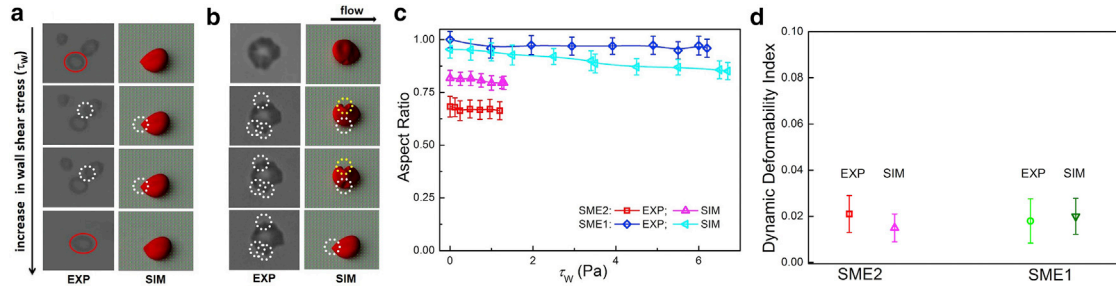


FIGURE 3 Detachment dynamics of sickle RBCs under the deoxygenated states. (a and b) Time sequence of adherent SME2 ((a) single-site attachment) and SME1 (b) multiple-site attachment) in response to applied shear stress obtained from experiments (left) and simulations (right). White and yellow dotted circles show the location of adhesion sites, and red circles highlight another adherent RBC nearby. In the last snapshot of the left figure, the adherent SME2 was washed away from the ROI after it detached from the substrate. (c) Functional dependence of the aspect ratio (AR) of sickle RBCs on the wall shear stress (WSS) τ_w . (d) Dynamic deformability index of sickle RBCs. The error bars in the figure show the statistical error of a set of measured AR and DDI values of RBCs at different pulse period. To see this figure in color, go online.

SME2s (single-site adhesion) and SME1s (multiple-site adhesion).

Single-site adhesion of SME2s. Fig. 3 a shows the snapshots of the detaching process of an SME2 with single-site adhesion. Compared to its counterpart in Fig. 2 b, the shape of the SME2 is not significantly affected under shear, and it maintains an oval shape until it detaches from the substrate wall.

Multiple-site adhesion of SME1s. Fig. 3 b shows snapshots of the shear-induced deformation of sickle RBCs corresponding to multiple-site adhesion under the deoxygenated state. From these experiments and simulations, we find that the SME1 exhibits localized membrane buckling in-between the apparent adhesion sites (see Fig. 3 b, white and yellow dotted circles). In addition, it does not deform continuously with the increase of WSS. Finally, the cell detaches from the substrate when the applied shear stress is above the threshold ($\tau_w^c \geq 6.7$ Pa (SIM)), which shows that SME1s under the deoxygenated state have stronger adhesion strength than their oxygenated counterparts. This result is also consistent with our previous study showing that hypoxia enhances the adhesion of SME1s (52).

Fig. 3, c and d show plots of the AR change and DDI values of SMEs. For both the SME1 and SME2, the AR value remains nearly constant under shear, leading to a quite low DDI value (Fig. 3 d). It is worth noting that for the simulation case of SME1, there is only a slight change in AR value (cyan left-pointing triangles in Fig. 3 c) when the weak adhesion site is ruptured at $\tau_w \approx 3.5$ Pa, possibly because of the cell membrane stiffening of SME1 under hypoxia.

Analysis of shear-induced deformation and surrounding fluid flow in cell detachment

It is known that hypoxia-induced sickling and cell membrane stiffening can alter the flow dynamics of sickle RBCs in shear flow (7,59). Hence, when the adherent

RBC is subjected to a pulsatile flow, the velocity field of its surrounding fluid flow changes significantly. Here, computational models provide a way to quantify the flow properties such as velocity and pressure fields with a good level of fidelity. For comparative analysis, we subjected the SME2 under the oxygenated and deoxygenated states to the same flow conditions and investigated the flow properties of the fluid particles around the SME2 (Fig. 4). We find that the velocity contours obtained from SME2s under the oxygenated state and the deoxygenated state are similar: the maximal velocity occurs at the centerline, and it

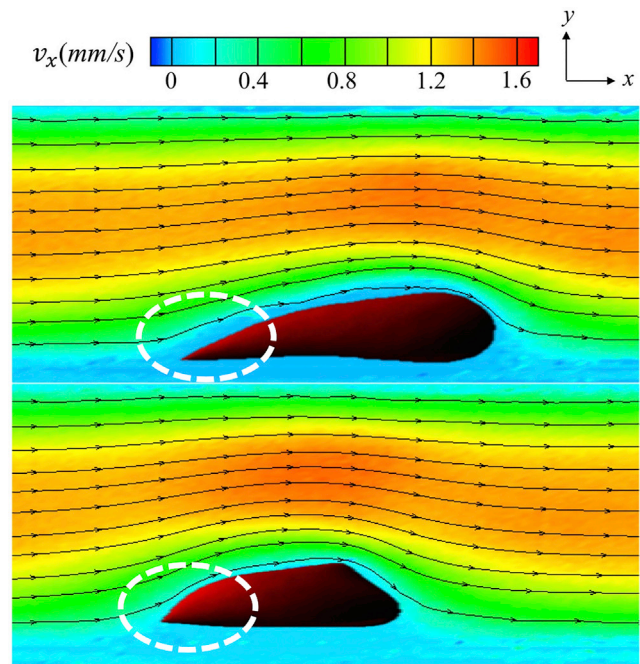


FIGURE 4 Velocity contours of fluid flow around sickle RBCs. In the plots, each arrow represents the direction of the fluid flow velocity. The white circles highlight the flow properties near the adhesion site of deformable SME2 (oxygenation; upper panel) and rigid SME2 (deoxygenation; lower panel). To see this figure in color, go online.

approaches to zero on the wall or near the cell membrane surface. The only difference between them is the velocity gradient around the cell membrane surface: the deformable SME2 (oxygenation) in shear flow undergoes dramatic changes in shape from an oblate to an elongated ellipsoid; hence, it shows a smooth velocity gradient along the longitudinal (major) axis of the deformed cell (Fig. 4, upper panel, dotted white circle). However, the rigid SME2 (deoxygenation) does not deform much even at high shear stress. This yields a steep velocity gradient at the near-wall region close to the cell membrane surface (in Fig. 4, lower panel, dotted white circle), resulting in an enhanced local shear stress around the RBC. Hence, under the same flow condition and system setup (i.e., same equilibrium cell shape and identical adhesive parameters), the rigid cell is always detached first from the substrate.

To further investigate the intrinsic mechanism, we plotted the average deformation, ϵ_i , on the cell membrane vertex i , given the following formula adapted from (67):

$$\epsilon_i = \sqrt{\frac{\sum_j^{N_i} \left(\frac{l_{ij}}{l_{ij,0}} - 1 \right)^2}{N_i}}, \quad (6)$$

where N_i represents the number of vertices directly associated to vertex i , l_{ij} , and $l_{ij,0}$ represent bond lengths between i and j under cell elongation and at equilibrium state, respectively. The corresponding deformation contours of the deformable SME2 (oxygenation) and rigid SME2 (deoxygenation) are presented in Fig. 5. Under the same system setup and flow condition, we observed a strong stress response at the membrane-fluid interface around the adhesion site. In addition, the magnitude of the deformation of the rigid SME2 (deoxygenation) is much higher than that of the deformable SME2 (oxygenation). As mentioned in the paragraph above, compared to the deformable SME2 (oxygenation), the rigid SME2 (deoxygenation) is subjected to stronger shear stress resulting from fluid flow. Another possible reason for this could stem from the different cell-substrate contact area (A_{cs}). In the current system, a differ-

ence in A_{cs} introduces a difference in F_{cs} . The deformable SME2 (oxygenation) shows a dramatic deformation under shear, causing a reduction in A_{cs} and F_{cs} . In contrast, the SME2 under the deoxygenated state is rigid by definition, so its behavior is consistent with this statement. The rigid SME2 (deoxygenation) exhibits a solid-like behavior, resulting in a relative larger A_{cs} and hence an enhanced F_{cs} .

Detachment dynamics of multiple RBCs with varied cell adhesions

Based on the previous experimental observations (64) and our aforementioned studies, we know that the strong adhesive bonds in weak-strong dual-binding strategy determines the behavior of RBC detaching from the substrate surface. Thus, our model can be well tailored for the detachment process of RBCs with single-site attachment, which is commonly observed and is critical in the detachment dynamics of RBCs. Also, the modeling of sickle cells with varied cell adhesion strength is more biomimetic, closer to those observed in in vivo studies.

We then present a simulation to accommodate a range of varied cell adhesion spring constants. Here, for illustrative purposes, we placed four sickle RBCs (with identical μ but different k_s) inside the microchannel and simulated their detachment dynamics under the pulsatile flow (Video S6). Our simulations show that the sickle RBCs with weaker adhesive bonds always detach earlier than those with stronger adhesive bonds (Fig. 6). In addition, when a flowing RBC (fully detached from the substrate) passes over an adhered one, both of these two RBCs exhibit local membrane deformations (Fig. 7). This is possibly due to the repulsion between the two interacting RBCs. Here, we only simulated four adherent cells in two separate microchannels, and we found that the cell-cell repulsive interaction play a significant role in cell detachment process. In addition, recent studies also suggest that cell-cell aggregation properties are likely to be involved in the pathophysiology of SCD (68). The aggregation MS-RBC model has been developed and employed to capture blood flow behavior by Fedosov

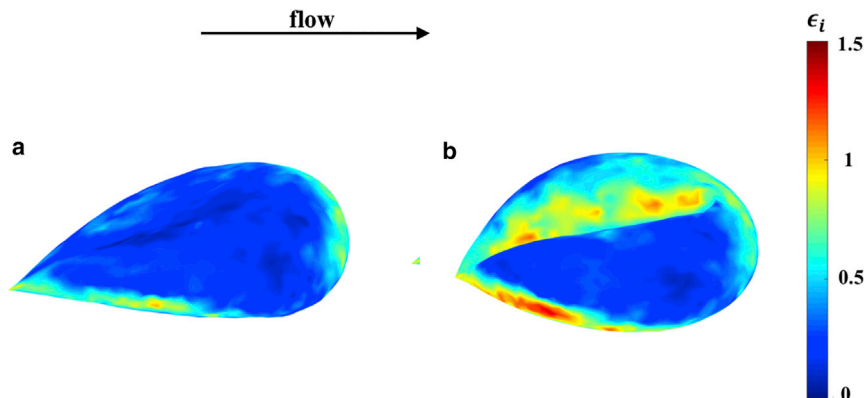


FIGURE 5 Average deformation contour of deformable SME2 ((a) oxygenation) and rigid SME2 ((b) deoxygenation) under shear. The flow direction is from left to right. To see this figure in color, go online.

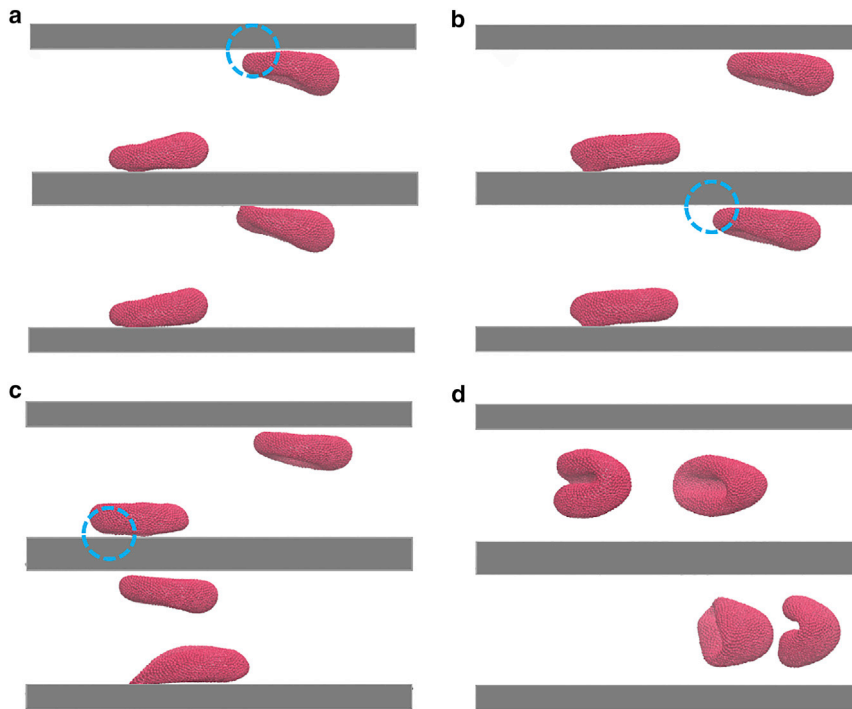


FIGURE 6 Sequential snapshots of the detachment dynamics of sickle RBCs (SME2s) for a range of varied cell adhesion spring constants. (a) $k_s = 4.8 \mu\text{N/m}$, (b) $48.0 \mu\text{N/m}$, (c) $96.0 \mu\text{N/m}$, and (d) $192.0 \mu\text{N/m}$. In the figure, the blue dashed circles denote the detachment instant. To see this figure in color, go online.

et al. (69). Here, explicit cell-cell aggregation interactions are not included in our simulations; this may be investigated more systematically in future studies.

CONCLUSIONS

In this work, we investigated both experimentally and computationally the RBC detachment dynamics under pulsatile flow conditions with increasing shear stress magnitude. We employed an in vitro microfluidic cell adherence assay to investigate the adhesion dynamics of SMEs and ISCs under well-controlled hypoxic conditions, inferring the cell adhesion strength by increasing the flow rate (or WSS) until the onset of cell detachment. In parallel, we employed a stochastic adhesion model in conjunction with the

dissipative particle dynamics method to model sickle cells and their interaction with the FN-coated surface. We performed detailed computational simulations with key model parameters derived from the microfluidic experiments, including flow rate, number of adhesion sites, cell shape, and deformability characteristics. After the experiments, we simulated both the deformable and rigid sickle RBCs with single- and multiple-site attachment. We found that the hypoxia-affected sickle RBCs (SME1s) under deoxygenated states show greater adhesion strength compared to their Oxy counterparts, indicating that hypoxia can significantly affect cell adhesive properties. We also simulated the detachment dynamics of a more complex system containing multiple RBCs, where the cell adhesion spring constant k_s was varied. We showed that the cell-cell interaction

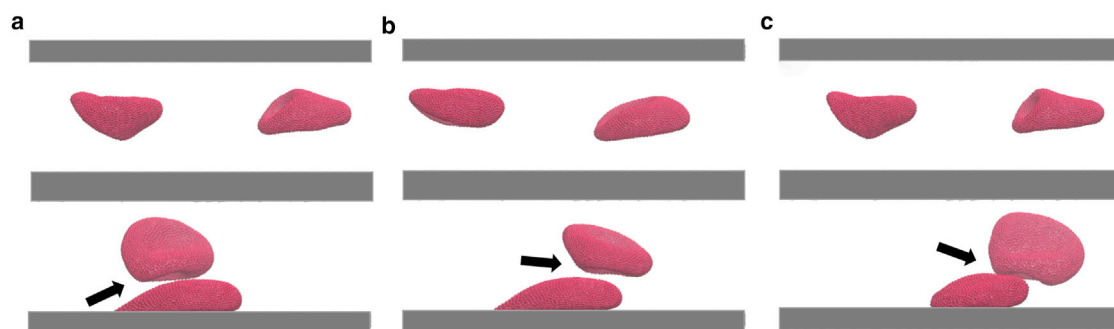


FIGURE 7 Shape deformation of two approaching sickle RBCs induced by a flowing RBC passing over an adherent RBC under shear. The sequential snapshots show the cell membrane deformation when the flowing RBC: (a) starts crossing the adherent one, (b) just after reaching the main body of the adherent one (c) approaches the end of the adherent one, causing its detachment from the substrate. Arrows indicate the local membrane deformation. To see this figure in color, go online.

also affects the detachment dynamics of adherent RBCs under shear flow. These findings will help us understand the effects of cell shape and membrane rigidity on cell adhesion under the pulsatile flow.

In our sickle cell adhesion model, some key adhesive parameters (such as the spring constant k_s for individual adhesion site) are informed by companion microfluidic experiments of RBC suspensions. Hence, our finding may not be applicable (at least directly) to whole blood adhesion and that FN may not directly be involved in the adhesive dynamics process in vivo (2,17). Such a limitation could be addressed in future work by conducting whole blood experiments to investigate cell-substrate adhesion properties of blood cells. In addition, it would require further developments of our simulation methods for the cell adhesion characterization to make future predictions more reliable. For example, the precise determination of cell surface adhesion properties is hard to be achieved experimentally; thus, it is not clear how functional adhesion properties are globally distributed on the individual cell's surface. Recent efforts have been directed toward this end. In a recent experimental study, Chemla and co-workers (70) developed a label-free cell surface adhesion mapping method to construct the functional maps of cell surface adhesion properties. This study provides a quantitative picture of cell surface adhesion at the functional and molecular level, which provides the possibility to simulate the specific adhesion patterns of individual RBCs. Such simulations from these disease-specific predictive models would be useful for characterizing the molecular and cellular mechanisms that contribute to cell-adhesion-related vaso-occlusion in SCD.

SUPPORTING MATERIAL

Supporting Materials and Methods, three figures, and six videos are available at [http://www.biophysj.org/biophysj/supplemental/S0006-3495\(18\)34503-X](http://www.biophysj.org/biophysj/supplemental/S0006-3495(18)34503-X).

AUTHOR CONTRIBUTIONS

Y.D., D.P.P., S.Z.A., H.-Y.C., X.L., M.D., and G.E.K. designed research. Y.D. and X.L. carried out the simulations. D.P.P. and S.Z.A. performed the experiments. X.L., M.D., and G.E.K. contributed new reagents/analysis tools. Y.D., D.P.P., S.Z.A., H.-Y.C., X.L., M.D., and G.E.K. analyzed data. Y.D., D.P.P., S.Z.A., H.-Y.C., X.L., M.D., and G.E.K. wrote the article.

ACKNOWLEDGMENTS

We thank Prof. Dr. Gregory J. Kato for providing sickle blood samples.

We acknowledge support from National Institutes of Health grants U01HL114476 and R01HL121386. X.L. acknowledges support from the Hundred Talents Program of Zhejiang University. An award of computer time was provided by the Advanced Scientific Computing Research Leadership Computing Challenge program. This research used resources of the Argonne Leadership Computing Facility, which is a Department of Energy Office of Science User Facility supported under contract DE-AC02-

06CH11357. This research also used resources of the Oak Ridge Leadership Computing Facility, which is a Department of Energy Office of Science User Facility supported under contract DE-AC05-00OR22725. D.P.P., S.Z.A., and M.D. have filed a patent based on the work presented in this article.

REFERENCES

- Bunn, H. F. 1997. Pathogenesis and treatment of sickle cell disease. *N. Engl. J. Med.* 337:762–769.
- Zhang, D., C. Xu, ..., P. S. Frenette. 2016. Neutrophils, platelets, and inflammatory pathways at the nexus of sickle cell disease pathophysiology. *Blood.* 127:801–809.
- Pauling, L., H. A. Itano, ..., I. C. Wells. 1949. Sickle cell anemia a molecular disease. *Science.* 110:543–548.
- Samuel, R. E., E. D. Salmon, and R. W. Briehl. 1990. Nucleation and growth of fibres and gel formation in sickle cell haemoglobin. *Nature.* 345:833–835.
- Kaul, D. K., M. E. Fabry, ..., R. L. Nagel. 1983. Erythrocytes in sickle cell anemia are heterogeneous in their rheological and hemodynamic characteristics. *J. Clin. Invest.* 72:22–31.
- Itoh, T., S. Chien, and S. Usami. 1995. Effects of hemoglobin concentration on deformability of individual sickle cells after deoxygenation. *Blood.* 85:2245–2253.
- Du, E., M. Diez-Silva, ..., S. Suresh. 2015. Kinetics of sickle cell bioreology and implications for painful vasoocclusive crisis. *Proc. Natl. Acad. Sci. USA.* 112:1422–1427.
- Li, X., E. Du, ..., G. E. Karniadakis. 2016. Patient-specific blood rheology in sickle-cell anaemia. *Interface Focus.* 6:20150065.
- Hosseini, P., S. Z. Abidi, ..., P. T. So. 2016. Cellular normoxic biophysical markers of hydroxyurea treatment in sickle cell disease. *Proc. Natl. Acad. Sci. USA.* 113:9527–9532.
- Hillery, C. A., M. C. Du, ..., J. P. Scott. 1996. Increased adhesion of erythrocytes to components of the extracellular matrix: isolation and characterization of a red blood cell lipid that binds thrombospondin and laminin. *Blood.* 87:4879–4886.
- Kaul, D. K., E. Finnegan, and G. A. Barabino. 2009. Sickle red cell-endothelium interactions. *Microcirculation.* 16:97–111.
- Kaul, D. K., M. E. Fabry, and R. L. Nagel. 1989. Microvascular sites and characteristics of sickle cell adhesion to vascular endothelium in shear flow conditions: pathophysiological implications. *Proc. Natl. Acad. Sci. USA.* 86:3356–3360.
- Hebbel, R. P., R. Osarogiagbon, and D. Kaul. 2004. The endothelial biology of sickle cell disease: inflammation and a chronic vasculopathy. *Microcirculation.* 11:129–151.
- Manwani, D., and P. S. Frenette. 2013. Vaso-occlusion in sickle cell disease: pathophysiology and novel targeted therapies. *Blood.* 122:3892–3898.
- Jimenez, M. A., E. Tutuncuoglu, ..., P. Sundd. 2015. Quantitative microfluidic fluorescence microscopy to study vaso-occlusion in sickle cell disease. *Haematologica.* 100:e390–e393.
- Bennewitz, M. F., S. C. Watkins, and P. Sundd. 2014. Quantitative intravital two-photon excitation microscopy reveals absence of pulmonary vaso-occlusion in unchallenged sickle cell disease mice. *Intravital.* 3:e29748.
- Bennewitz, M. F., M. A. Jimenez, ..., P. Sundd. 2017. Lung vaso-occlusion in sickle cell disease mediated by arteriolar neutrophil-platelet microemboli. *JCI Insight.* 2:e89761.
- Barabino, G. A., M. O. Platt, and D. K. Kaul. 2010. Sickle cell biomechanics. *Annu. Rev. Biomed. Eng.* 12:345–367.
- Li, X., M. Dao, ..., G. E. Karniadakis. 2017. Biomechanics and bioreology of red blood cells in sickle cell anemia. *J. Biomech.* 50:34–41.
- Wautier, J. L., F. Galacteros, ..., J. P. Caen. 1985. Clinical manifestations and erythrocyte adhesion to endothelium in sickle cell syndrome. *Am. J. Hematol.* 19:121–130.

21. Kaul, D. K., D. Chen, and J. Zhan. 1994. Adhesion of sickle cells to vascular endothelium is critically dependent on changes in density and shape of the cells. *Blood*. 83:3006–3017.
22. Alapan, Y., J. A. Little, and U. A. Gurkan. 2014. Heterogeneous red blood cell adhesion and deformability in sickle cell disease. *Sci. Rep.* 4:7173.
23. Pivkin, I. V., P. D. Richardson, and G. Karniadakis. 2006. Blood flow velocity effects and role of activation delay time on growth and form of platelet thrombi. *Proc. Natl. Acad. Sci. USA*. 103:17164–17169.
24. Pothapragada, S., P. Zhang, ..., D. Bluestein. 2015. A phenomenological particle-based platelet model for simulating filopodia formation during early activation. *Int. J. Numer. Methods Biomed. Eng.* 31: e02702.
25. Vahidkhah, K., and P. Bagchi. 2015. Microparticle shape effects on margination, near-wall dynamics and adhesion in a three-dimensional simulation of red blood cell suspension. *Soft Matter*. 11:2097–2109.
26. Zhang, P., L. Zhang, ..., D. Bluestein. 2017. A multiscale biomechanical model of platelets: correlating with *in-vitro* results. *J. Biomech.* 50:26–33.
27. Li, X., H. Li, ..., G. E. Karniadakis. 2017. Computational biomechanics of human red blood cells in hematological disorders. *J. Biomech. Eng.* 139:021008.
28. Bell, G. I. 1978. Models for the specific adhesion of cells to cells. *Science*. 200:618–627.
29. Dembo, M. 1994. On peeling an adherent cell from a surface. In *Lectures on Mathematics in the Life Sciences, Some Mathematical Problems in Biology, Volume 24*. American Mathematical Society, pp. 51–77.
30. Hammer, D. A., and S. M. Apte. 1992. Simulation of cell rolling and adhesion on surfaces in shear flow: general results and analysis of selectin-mediated neutrophil adhesion. *Biophys. J.* 63:35–57.
31. Jadhav, S., C. D. Eggleton, and K. Konstantopoulos. 2005. A 3-D computational model predicts that cell deformation affects selectin-mediated leukocyte rolling. *Biophys. J.* 88:96–104.
32. Walton, E. B., S. Lee, and K. J. Van Vliet. 2008. Extending Bell's model: how force transducer stiffness alters measured unbinding forces and kinetics of molecular complexes. *Biophys. J.* 94:2621–2630.
33. Fedosov, D. A., B. Caswell, and G. E. Karniadakis. 2011. Wall shear stress-based model for adhesive dynamics of red blood cells in malaria. *Biophys. J.* 100:2084–2093.
34. Ye, H., Z. Shen, and Y. Li. 2018. Cell stiffness governs its adhesion dynamics on substrate under shear flow. *IEEE Trans. NanoTechnol.* 17:407–411.
35. Yang, Y., and H. Jiang. 2018. Cellular volume regulation and substrate stiffness modulate the detachment dynamics of adherent cells. *J. Mech. Phys. Solids*. 112:594–618.
36. Li, H., and G. Lykotrafitis. 2012. Two-component coarse-grained molecular-dynamics model for the human erythrocyte membrane. *Biophys. J.* 102:75–84.
37. Li, H., and G. Lykotrafitis. 2014. Erythrocyte membrane model with explicit description of the lipid bilayer and the spectrin network. *Biophys. J.* 107:642–653.
38. Tang, Y. H., L. Lu, ..., G. E. Karniadakis. 2017. OpenRBC: a fast simulator of red blood cells at protein resolution. *Biophys. J.* 112:2030–2037.
39. Li, H., L. Lu, ..., S. Suresh. 2018. Mechanics of diseased red blood cells in human spleen and consequences for hereditary blood disorders. *Proc. Natl. Acad. Sci. USA*. 115:9574–9579.
40. Li, H., V. Ha, and G. Lykotrafitis. 2012. Modeling sickle hemoglobin fibers as one chain of coarse-grained particles. *J. Biomech.* 45:1947–1951.
41. Lu, L., X. Li, ..., G. E. Karniadakis. 2016. Probing the twisted structure of sickle hemoglobin fibers via particle simulations. *Biophys. J.* 110:2085–2093.
42. Lu, L., H. Li, ..., G. E. Karniadakis. 2017. Mesoscopic adaptive resolution scheme toward understanding of interactions between sickle cell fibers. *Biophys. J.* 113:48–59.
43. Pivkin, I. V., and G. E. Karniadakis. 2008. Accurate coarse-grained modeling of red blood cells. *Phys. Rev. Lett.* 101:118105.
44. Fedosov, D. A., B. Caswell, and G. E. Karniadakis. 2010. A multiscale red blood cell model with accurate mechanics, rheology, and dynamics. *Biophys. J.* 98:2215–2225.
45. Lei, H., and G. E. Karniadakis. 2012. Quantifying the rheological and hemodynamic characteristics of sickle cell anemia. *Biophys. J.* 102:185–194.
46. Lei, H., and G. E. Karniadakis. 2013. Probing vasoocclusion phenomena in sickle cell anemia via mesoscopic simulations. *Proc. Natl. Acad. Sci. USA*. 110:11326–11330.
47. Maciaszek, J. L., B. Andemariam, ..., G. Lykotrafitis. 2014. AKAP-dependent modulation of BCAM/Lu adhesion on normal and sickle cell disease RBCs revealed by force nanoscopy. *Biophys. J.* 106: 1258–1267.
48. Zhang, J., K. Abiraman, ..., B. Andemariam. 2017. Regulation of active ICAM-4 on normal and sickle cell disease RBCs via AKAPs is revealed by AFM. *Biophys. J.* 112:143–152.
49. Kucukal, E., J. A. Little, and U. A. Gurkan. 2018. Shear dependent red blood cell adhesion in microscale flow. *Integr. Biol.* 10:194–206.
50. Alapan, Y., Y. Matsuyama, ..., U. A. Gurkan. 2016. Dynamic deformability of sickle red blood cells in microphysiological flow. *Technology (Singap World Sci)*. 4:71–79.
51. Kim, M., Y. Alapan, ..., U. A. Gurkan. 2017. Hypoxia-enhanced adhesion of red blood cells in microscale flow. *Microcirculation*. 24:e12374.
52. Papageorgiou, D. P., S. Z. Abidi, ..., M. Dao. 2018. Simultaneous polymerization and adhesion under hypoxia in sickle cell disease. *Proc. Natl. Acad. Sci. USA*. 115:9473–9478.
53. Zheng, Y., M. A. Cachia, ..., Y. Sun. 2015. Mechanical differences of sickle cell trait (SCT) and normal red blood cells. *Lab Chip*. 15:3138–3146.
54. Lipowsky, H. H., S. Kovalcheck, and B. W. Zweifach. 1978. The distribution of blood rheological parameters in the microvasculature of cat mesentery. *Circ. Res.* 43:738–749.
55. Smith, B. D., and P. L. La Celle. 1986. Erythrocyte-endothelial cell adherence in sickle cell disorders. *Blood*. 68:1050–1054.
56. Peng, Z., X. Li, ..., S. Suresh. 2013. Lipid bilayer and cytoskeletal interactions in a red blood cell. *Proc. Natl. Acad. Sci. USA*. 110:13356–13361.
57. Pivkin, I. V., Z. Peng, ..., S. Suresh. 2016. Biomechanics of red blood cells in human spleen and consequences for physiology and disease. *Proc. Natl. Acad. Sci. USA*. 113:7804–7809.
58. Fedosov, D. A., B. Caswell, ..., G. E. Karniadakis. 2011. Quantifying the biophysical characteristics of *Plasmodium-falciparum*-parasitized red blood cells in microcirculation. *Proc. Natl. Acad. Sci. USA*. 108:35–39.
59. Li, X., E. Du, ..., G. E. Karniadakis. 2017. Patient-specific modeling of individual sickle cell behavior under transient hypoxia. *PLoS Comput. Biol.* 13:e1005426.
60. Chang, H. Y., X. Li, ..., G. E. Karniadakis. 2016. MD/DPD multiscale framework for predicting morphology and stresses of red blood cells in health and disease. *PLoS Comput. Biol.* 12:e1005173.
61. Chang, H. Y., X. Li, and G. E. Karniadakis. 2017. Modeling of biomechanics and biorheology of red blood cells in type 2 diabetes mellitus. *Biophys. J.* 113:481–490.
62. Chang, H. Y., A. Yazdani, ..., G. E. Karniadakis. 2018. Quantifying platelet margination in diabetic blood flow. *Biophys. J.* 115:1371–1382.
63. Pivkin, I. V., and G. E. Karniadakis. 2006. Controlling density fluctuations in wall-bounded dissipative particle dynamics systems. *Phys. Rev. Lett.* 96:206001.
64. Kasschau, M. R., G. A. Barabino, ..., D. E. Golan. 1996. Adhesion of sickle neutrophils and erythrocytes to fibronectin. *Blood*. 87:771–780.

65. Lomholt, S., and M. R. Maxey. 2003. Force-coupling method for particulate two-phase flow: Stokes flow. *J. Comput. Phys.* 184:381–405.
66. Lei, H., and G. E. Karniadakis. 2012. Predicting the morphology of sickle red blood cells using coarse-grained models of intracellular aligned hemoglobin polymers. *Soft Matter*. 8:4507–4516.
67. Xiao, L. L., Y. Liu, ..., B. M. Fu. 2016. Numerical simulation of a single cell passing through a narrow slit. *Biomech. Model. Mechanobiol.* 15:1655–1667.
68. Tripette, J., T. Alexy, ..., P. Connes. 2009. Red blood cell aggregation, aggregate strength and oxygen transport potential of blood are abnormal in both homozygous sickle cell anemia and sickle-hemoglobin C disease. *Haematologica*. 94:1060–1065.
69. Fedosov, D. A., W. Pan, ..., G. E. Karniadakis. 2011. Predicting human blood viscosity in silico. *Proc. Natl. Acad. Sci. USA*. 108:11772–11777.
70. Li, I. T., T. Ha, and Y. R. Chemla. 2017. Mapping cell surface adhesion by rotation tracking and adhesion footprinting. *Sci. Rep.* 7:44502.
71. Dembo, M., D. C. Torney, ..., D. Hammer. 1988. The reaction-limited kinetics of membrane-to-surface adhesion and detachment. *Proc. R. Soc. Lond. B Biol. Sci.* 234:55–83.
72. Marshall, B. T., K. K. Sarangapani, ..., C. Zhu. 2006. Measuring molecular elasticity by atomic force microscope cantilever fluctuations. *Biophys. J.* 90:681–692.
73. Schwarz, U. S., and R. Alon. 2004. L-selectin-mediated leukocyte tethering in shear flow is controlled by multiple contacts and cytoskeletal anchorage facilitating fast rebinding events. *Proc. Natl. Acad. Sci. USA*. 101:6940–6945.
74. Alon, R., S. Chen, ..., T. A. Springer. 1997. The kinetics of L-selectin tethers and the mechanics of selectin-mediated rolling. *J. Cell Biol.* 138:1169–1180.

Biophysical Journal, Volume 116

Supplemental Information

**Quantifying Shear-Induced Deformation and Detachment of Individual
Adherent Sickle Red Blood Cells**

**Yixiang Deng, Dimitrios P. Papageorgiou, Hung-Yu Chang, Sabia Z. Abidi, Xuejin Li, Ming
Dao, and George Em Karniadakis**

Supporting Information: Quantifying shear-induced deformation and detachment of individual adherent sickle red blood cells

Y. Deng, D. P. Papageorgiou, H.-Y. Chang, S. Z. Abidi, X. Li, M. Dao, G. E. Karniadakis

Verification for benchmark problem

In the simulation of oscillating flow using the force coupling method (FCM), we imposed a time-dependent oscillating pressure gradient along the flow direction. For DPD simulations, an equivalent time-varying body force is exerted on the fluid particles containing the microbead particle. In both cases, periodic velocity boundary conditions are implemented in x and z directions, while bounce-back and solid wall boundary condition is used in y direction. In Fig. S1, we show the displacement of an oscillating microbead particle from its equilibrium position (d^* ; normalized by its amplitude) and the input pressure profile (p^* ; normalized by the maximum value) that obtained from DPD and FCM simulations. In those figures, the companion experimental data for particle displacement are shown. From Fig. S1, we find that our computed curves are in good agreement with the measured data, except that near the peak domains a visible discrepancy in the displacement profiles is noticed. However, when we compared our computational curves with those obtained from FCM modeling, we obtained an excellent agreement. Herein, the hydrodynamic fluid flow with suspended particle can be simply and accurately implemented through the DPD approach.

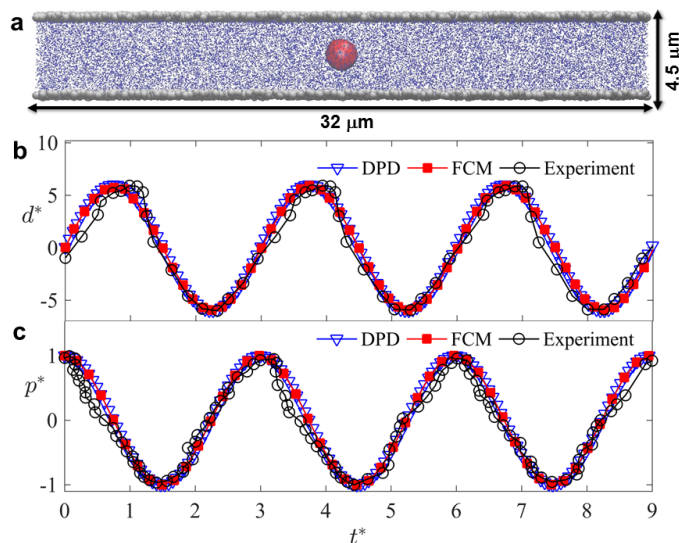


Figure S1. Simulation of an oscillating microbead particle in response to an oscillating pressure. (a) Schematic representation of a microbead particle in microchannel. (b) Displacement of an oscillating microbead particle from its equilibrium position, and (c) the input pressure profile. The empty triangles and solid squares show the computational results obtained from DPD and FCM numerical simulations, and the empty circles show the measured data in experiments.

Mechanical attachment of individual sickle RBCs under shear

We coated the entire lower wall with ligand particles to enable successive adhesion and detachment (Fig. S2a). We studied the attachment dynamics of sickle RBCs under Poiseuille's flow for different cell adhesion

strength constant k_s , varying in $1.92 \mu\text{N/m}$, $4.80 \mu\text{N/m}$, and $19.2 \mu\text{N/m}$. When we applied the same pressure gradient in four cases, two distinct behaviors are observed – rolling and flipping. Here we regard firm adhesion as a flipping dynamics with infinite flipping period and treading as flipping with an observable period. Fig. S2*b* shows the RBC displacement (upper) and instantaneous cell velocity (lower) of different dynamics behaviors. After first contact with the lower wall, several different dynamic behavior were observed (see Fig. S2*a*), including rolling, treading, firm adhesion and another interesting intermediate behavior, flip once or say treading with a relatively long period, which can be quantified by the time intervals between neighboring velocity peaks, see Fig. S2*b*.

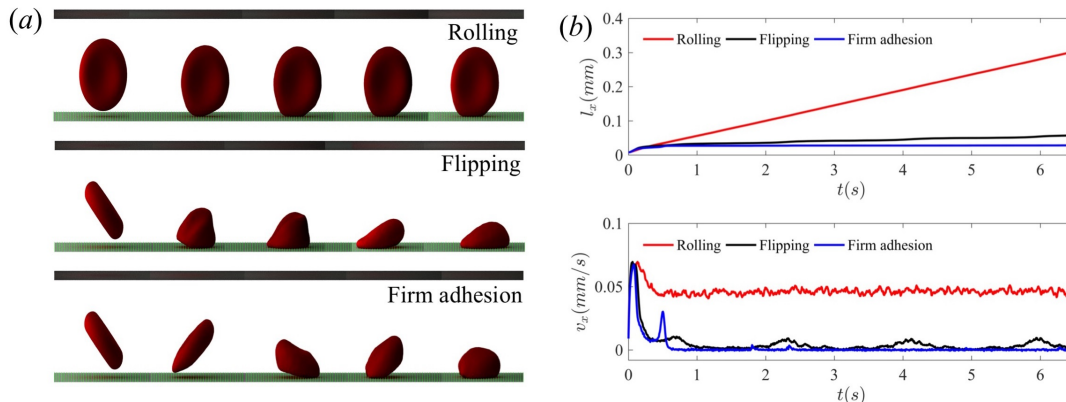


Figure S2. Adhesion dynamics of sickle RBCs under shear flow. (a) heterogeneous attachment dynamics with different initial geometrical settings and adhesion spring constant k_s . From top to bottom are RBC rolling ($k_s = 1.92 \mu\text{N/m}$), flipping ($k_s = 4.80 \mu\text{N/m}$), and firm adhesion ($k_s = 19.2 \mu\text{N/m}$); (b) displacement evolution and velocity evolution of cells with rolling, flipping and firm adhesion dynamics.

Mechanical detachment of sickle RBC suspension under shear

We investigated the detachment dynamics of sickle RBC suspension under linear flow, with the increase of the magnitude of wall shear stress. The cumulative histogram for the observed detachment events of sickle RBCs is shown in Fig. S3, from which we found that the sickle RBCs may detach from the surface under shear stress conditions from low to high.

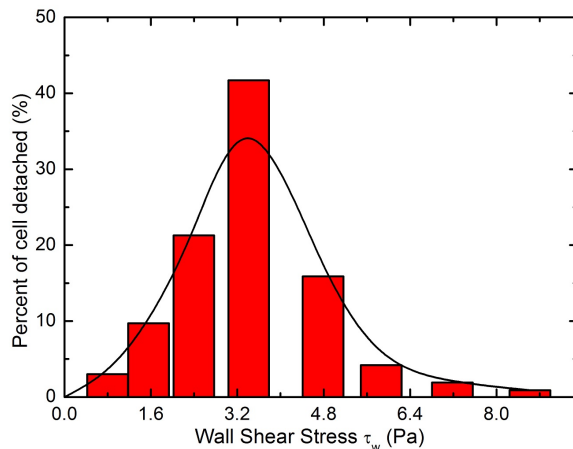
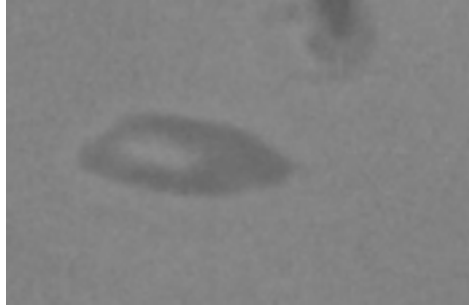


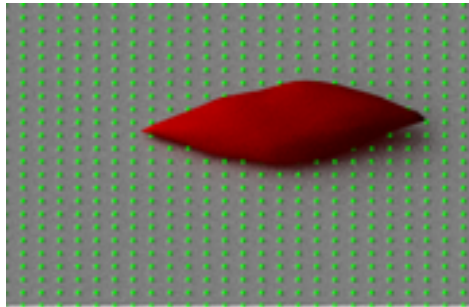
Figure S3. Cumulative histogram for the observed detachment events of sickle RBCs under shear.

Supporting videos

S1 Video: Experimental observation of detachment dynamics of an ISC (single-site attachment) under the Oxy condition.



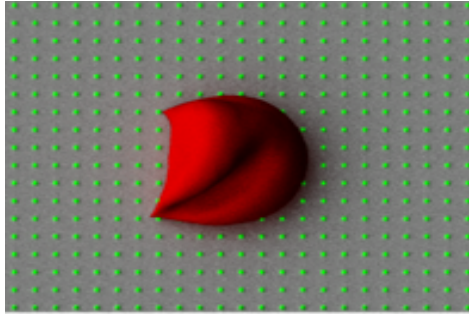
S2 Video: Simulation of detachment dynamics of a modeled ISC (single-site attachment) under the Oxy condition.



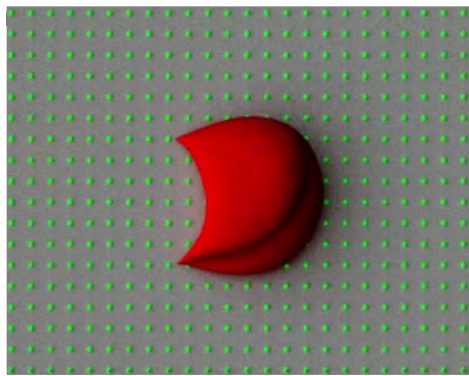
S3 Video: Experimental observation of detachment dynamics of an SME1 (multiple-site attachment) under the Oxy condition.



S4 Video: Simulation of detachment dynamics of a modeled SME1 (multiple-site attachment; $k_s^{wk} = 0.50k_s^{st}$) under the Oxy condition.



S5 Video: Simulation of detachment dynamics of a modeled SME1 (multiple-site attachment; $k_s^{wk} = 0.75k_s^{st}$) under the Oxy condition.



S6 Video: Simulation of detachment dynamics of sickle RBCs (SME2s) for a range of varied cell adhesion spring constant k_s .

